Available online at www.sciencedirect.com
ScienceDirect
Trans. Nonferrous Met. Soc. China 35(2025) 613−624
Transactions of Nonferrous Metals Society of China
www.tnmsc.cn

Process, influence factors and mechanism of direct generation of zinc metal using laser to irradiate ZnS

Ying CHEN[1,2], Ning DUAN[1,2], Lin-hua JIANG[1,2], Hao JIN[1,2], Yao WANG[1,2], Yong LIU[1,2]

1. State Key Laboratory of Pollution Control and Resources Reuse, College of Environmental Science and Engineering, Tongji University, Shanghai 200092, China;
2. Shanghai Institute of Pollution Control and Ecological Security, Shanghai 200092, China

Received 3 June 2024; accepted 27 December 2024

Abstract: The generation process, influence of the laser parameters on the production of zinc metal (Zn^0), and the mechanism of interaction between the laser and ZnS were studied. It was observed that an increase in the number of S defects enhanced the quantity of Zn^{2+} ejected from the ZnS crystals, which increased the possibility of Zn^{2+} bonding with electrons to produce Zn^0. A maximum Zn^0 content of 9.3% in the products was detected upon changing the laser parameters. Upon analyzing the changes in the surface topography during the laser interaction with ZnS, it was shown that the interaction mechanism between laser and ZnS had a synergistic effect comprised of photochemical and photothermal processes, in which the photochemical mechanism predominated.

Key words: laser metallurgy; sulfur defects; surface topography; photochemical reduction; zinc metal

1 Introduction

China's carbon dioxide emissions have increased 3.35-fold over 22 years, from 292.386×10^6 t in 1997 to 979.476×10^6 t in 2019, as reported by the Intergovernmental Panel on Climate Change (IPCC) [1,2]. Aiming to reduce carbon emissions and meet the environmental challenges caused by climate change, the Chinese government put forward the goal of reaching a carbon emission peak by 2030 and achieving carbon neutrality by 2060 [3]. Its relevant national departments issued an Implementation Plan for Carbon Peaking in the Non-ferrous Metals Industry, which put forward that the non-ferrous metal industry shall achieve the target of carbon peak by 2025 [4]. Therefore, in order to achieve its dual carbon goals, there is an urgent task to reduce CO_2 emissions from the non-ferrous industry.

Zinc is the fourth most extensively employed metal at present, with a global usage of up to 13.7×10^6 t in 2023 alone [5]. Its ultimate utility extends across the automotive, architectural, maritime, culinary, electronic, biotechnological, pharmaceutical, cosmetic, and other pertinent industries [6]. Sphalerite is the primary raw material used in the electrolytic zinc industry and its main, and efficient component is ZnS [7,8]. The production of electrolytic zinc is a long process that includes many production units and its final product is zinc metal (Zn^0). The first unit in this long process is high temperature roasting, which produces a large amount of CO_2. In 2020, the comprehensive carbon dioxide emissions generated during the production of one ton of zinc metallurgy industry in China amounted to 5.19 t, which is equivalent to the consumption of 1.9 t of standard

Corresponding author: Ning DUAN: Tel: +86-13801014910, E-mail: ningduan2020@163.com;
Lin-hua JIANG: Tel: +86-13269367132, E-mail: jianglinhuann@163.com
DOI: https://doi.org/10.1016/S1003-6326(24)66703-8

coal. Meanwhile, the zinc industry emits a total of 33×10^6 t of CO_2, which places a heavy burden on the environment.

Researchers have been developing a diverse range of technologies in order to reduce carbon emissions in the electrolytic zinc process [9]. Microwave heating provides higher heating rates than conventional zinc metallurgy methods, which results in reduced heating time, energy consumption, and carbon emissions [10]. A nearly complete reduction of ZnO and zinc volatilization can be accomplished using wood biomass for the reduction reaction. When compared to fossil fuels, wood biomass exhibits a higher reducing capacity and contributes to reducing CO_2 emissions [11]. Vacuum metallurgy is a clean and efficient metallurgical technology operated in a confined system below atmospheric pressure, which has rapidly developed in areas such as metal separation and purification, and hazardous waste treatment [12]. Despite the progress made during the long-term efforts of researchers toward developing various technologies, the results of these technologies fall short of achieving the necessary reduction in carbon emissions for carbon neutrality, especially in the electrolytic zinc industry.

Laser-induced techniques for reducing metal ions to elemental metals generally follow two main pathways: The first involves direct laser-induced deposition in metal ion solutions, in which laser irradiation of the metal ion precursor solution leads to the photochemical reduction of metal ions via two-photon absorption, resulting in the formation of metal nanostructures either in the solution or directly on a metal surface [13]. The second pathway involves the reduction of metal ions within a carrier structure containing metal ions or the direct laser-induced reduction of solid materials to convert metal ions into elemental metals [14,15]. DU et al [16] studied the interaction between the laser source and tin concentrate. In this study, tin metal was directly detected by uniformly scanning the entire tin concentrate powder with a laser. JIANG et al [17] explored nanoscale laser metallurgy. In their research, a laser was used to accurately delivered patches of highly concentrated energy to the metal ions in the crystals of metal-organic frameworks (MOF), which were transformed into carbonaceous organic linkers, resulting in the formation of reductive species, and in turn, reduce the metal ions into atoms.

In this work, we have developed a prototype optical metallurgy method for zinc metal, which utilized laser-induced ZnS to directly generate zinc metal to nearly eradicate the carbon emissions generated by the electrolytic production of Zn [18]. This method, although in its primary stage, exhibited great potential for carbon neutrality as it completely removed the need for the high-temperature roasting process (850 °C or higher) used in the traditional zinc metal industry.

The generation process, influence of laser parameters on the production of Zn^0 and interaction mechanism between the laser and ZnS were further studied. When irradiated by a laser, the ZnS crystal initially ejected S^{2-} followed by Zn^{2+} ejection. Zn^{2+} combined with the free electrons to form Zn^0. Laser fluences, pulse repetition frequencies, and scan spacing were important factors affecting the production of Zn^0. The appropriate selection and combination of parameters have a bright future to obtain more Zn^0 from laser induced ZnS. Photochemical and photothermal processes coexisted in the production of Zn^0 with the photochemical process being dominant.

2 Experimental

2.1 Materials

The material used in this experiment was a single crystal ZnS wafer with 99.9% purity, purchased from Guangzhou Hengyang Electronic Technology Co., Ltd. It had a regular circular shape with a diameter of 12.7 mm and thickness of 2 mm.

2.2 Characterization

Information regarding the crystalline structure of laser-irradiated ZnS was obtained using high-resolution transmission electron microscopy (HRTEM, FEI Tecnai F20). The surface chemical composition and surface topography of ZnS after laser irradiation were characterized using energy dispersive X-ray spectroscopy (EDS) and scanning electron microscopy (SEM, ZEISS Gemini SEM 300). Electron paramagnetic resonance (EPR) spectroscopy (Bruker EMXplus) was conducted to study the S defects in ZnS. Information regarding the crystalline and phase of unirradiated ZnS was obtained using X-ray diffraction (XRD; Bruker D8 Advance). X-ray photoelectron spectroscopy (XPS)

was used to analyze the chemical state of ZnS after laser irradiation. Simultaneously, Raman spectroscopy was performed at room temperature using a Renishaw in Via laser Raman spectrometer with an excitation wavelength of 515 nm.

2.3 Decomposition of laser-induced ZnS

Figure 1 shows that the entire experimental platform mainly consists of three parts: optical system, control system, and mechanical system. The optical system primarily included the laser, beam expander, dynamic focusing lens assembly, reflector, galvanometer scanner, lens, and CCD camera. Details of the laser-induced decomposition of the ZnS experiment are presented in Text S1 in the Supporting Information (SI).

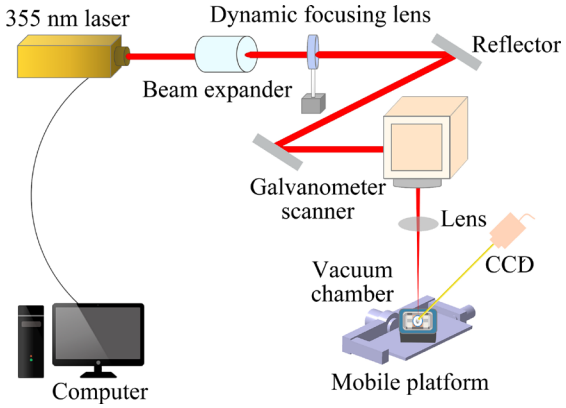

Fig. 1 Diagram of laser-induced decomposition setup used for ZnS experiment

Ultraviolet-visible near-infrared diffuse reflectance spectroscopy showed that ZnS exhibits a relatively high photoresponse in the ultraviolet light region, particularly in the wavelength range of 290−360 nm, displaying high light-absorption capability [19,20]. Furthermore, density functional theory (DFT) calculations and photoelectric effect analysis revealed that the optimal excitation wavelength for ZnS was 337 nm [18]. Due to the limited availability of 337 nm ultraviolet lasers in the market, a 355 nm nanosecond pulsed ultraviolet laser (OPTOWAVE Co. Ltd., USA) was used in this experiment and details of the laser parameters are provided in Text S2 in SI.

It has been observed that the laser fluence (F) has a more noticeable impact on the microstructure of the ZnS surface [18]. Orthogonal experimental design is an economical and accessible method; however, its results may be influenced by the interaction of multiple factors, leading to uncertain or ambiguous conclusions [21]. To further investigate the effects of the laser parameters on the Zn^0 content in the products in detail as well as their impact on the surface topography and chemical composition changes of ZnS, single-factor experiments were conducted on the three most influential factors: pulse repetition frequency (f), scan spacing, and F, while keeping all the other parameters constant (scanning speed, 300 mm/s; light spot diameter, 40 μm). Meanwhile, given the laser damage threshold of ZnS and considering the absorption and reflection of light when the laser passes through the vacuum chamber, which resulted in the partial loss of laser energy, the laser parameters utilized in the experiment were determined, as shown in Table S1 in SI.

3 Results and discussion

3.1 Generation process of Zn^0 under laser irradiation

When the laser irradiated ZnS, it induced electron transition in ZnS, which led to the breakage of the ZnS bond, resulting in the decomposition of ZnS. As ZnS is a semiconductor, Zn^{2+}, S^{2-}, and free electrons are produced when it is decomposed by laser irradiation. In diatomic molecules, when the thermal excitation reaches a certain level, the atoms with a lower atomic mass typically have higher vibration frequencies and lower excitation energies, making them more likely to overcome energy barriers and be excited from the crystal [22]. As the relative atomic mass of the S atom is much smaller than that of Zn, S^{2-} will be ejected first from the ZnS crystal and generate S defects. When S^{2-} is ejected up to a certain amount, Zn^{2+} will then be ejected from the ZnS crystal. Subsequently, Zn^{2+} will combine with the free electrons to form Zn^0 under the protection of an inert argon gas atmosphere.

To confirm the Zn^0 generation process, ZnS samples before and after laser irradiation were exposed to air for some time, and the changes in the surface chemical composition were explored using EDS. The regional distribution of the different elements is shown in Fig. 2, which mainly included Zn, S, O and C. C on the wafer surface primarily resulted from the adhesion of organic compounds from the air before EDS analysis, as well as the

residual organic compounds present in the EDS instrument [23]. O on the wafer surface originated from the adsorption of oxygen molecules in the air, while Zn and S were entirely derived from the substrate.

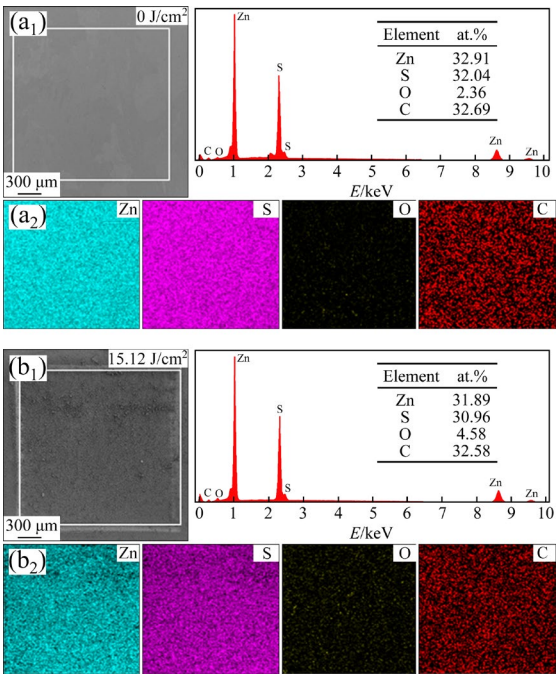

Fig. 2 EDS mapping images of ZnS before and after laser irradiation: (a_1, a_2) Before irradiation; (b_1, b_2) After irradiation

Figure 2 shows the elemental content in numerals and colors. The numerals of the elemental content are listed on the right of Figs. 2(a_1) and (b_1). The colors of the elemental content are shown in the small figures of Figs. 2(a_2) and (b_2). The darker the small figures, the lower the content of the targeted element [24]. When comparing Figs. 2(a_1) and (b_1), it was found that after laser irradiation the O content on the ZnS surface increased dramatically, while the C content remained almost unchanged, and at the same time, the amount of Zn and S both decreases. This demonstrated that laser irradiation decomposed ZnS so that more O and C elements appeared on the surface of ZnS, reducing the density of Zn and S on the surface of ZnS. However, as mentioned before, O was adsorbed, while C adhered on the surface of ZnS, which explained why the O content increased faster than the C content.

Figure 3 further explains the generation process for Zn^0. C was removed for better observation of the changes in the Zn, S, and O contents. The remaining elements were normalized and analyzed, as shown in Fig. 3. This figure lists the results of the experiment using a laser operated at different laser fluences and pulse repetition frequencies to irradiate the ZnS wafer. In each experiment the Zn content was higher than that of S. This result coincided very well with the process described above; the S atom was lighter so it was ejected first, and the quantity ejected was more than that of Zn, hence, there was more Zn element on the wafer surface.

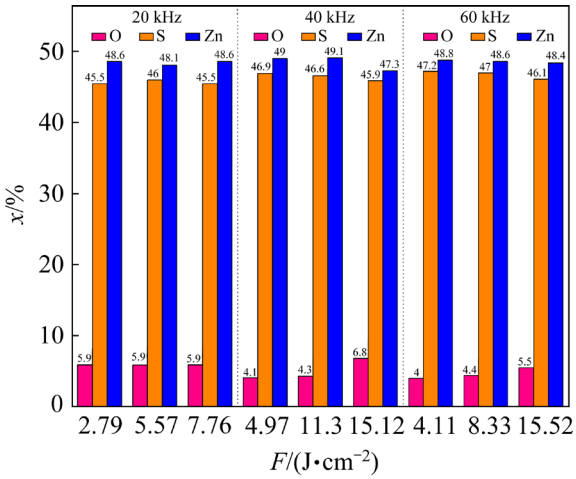

Fig. 3 Distribution of Zn, S and O contents under different pulse repetition frequencies and laser fluences

Figure 4 provides more details regarding the Zn^0 generation process using the results obtained from XPS, EPR, and HRTEM analyses. In the S 2p region, the peaks were symmetrical with spin-orbit splitting. Figure 4(a) shows that when compared to unirradiated ZnS, at an identical *f*, all of the binding energies (161.6 eV) of S 2p progressively transferred to a comparatively higher binding energy (163.3 eV) with an increase in the *F* level, suggesting that more and more S vacancies on ZnS crystals were created and more and more S^{2-} was ejected [25]. The reason for this was that when the laser interacted with ZnS, irradiation resulted in electron transfer from ZnS to the S vacancies, which reduced the electron cloud density around S and thus shifted the binding energy of the S 2p orbitals positively [26].

The presence of surface S vacancies alters the electronic structure of atoms around the S vacancies, which enhances the adsorption activity on the ZnS surface, increasing the oxygen content [27,28]. It has been demonstrated that a significant number of

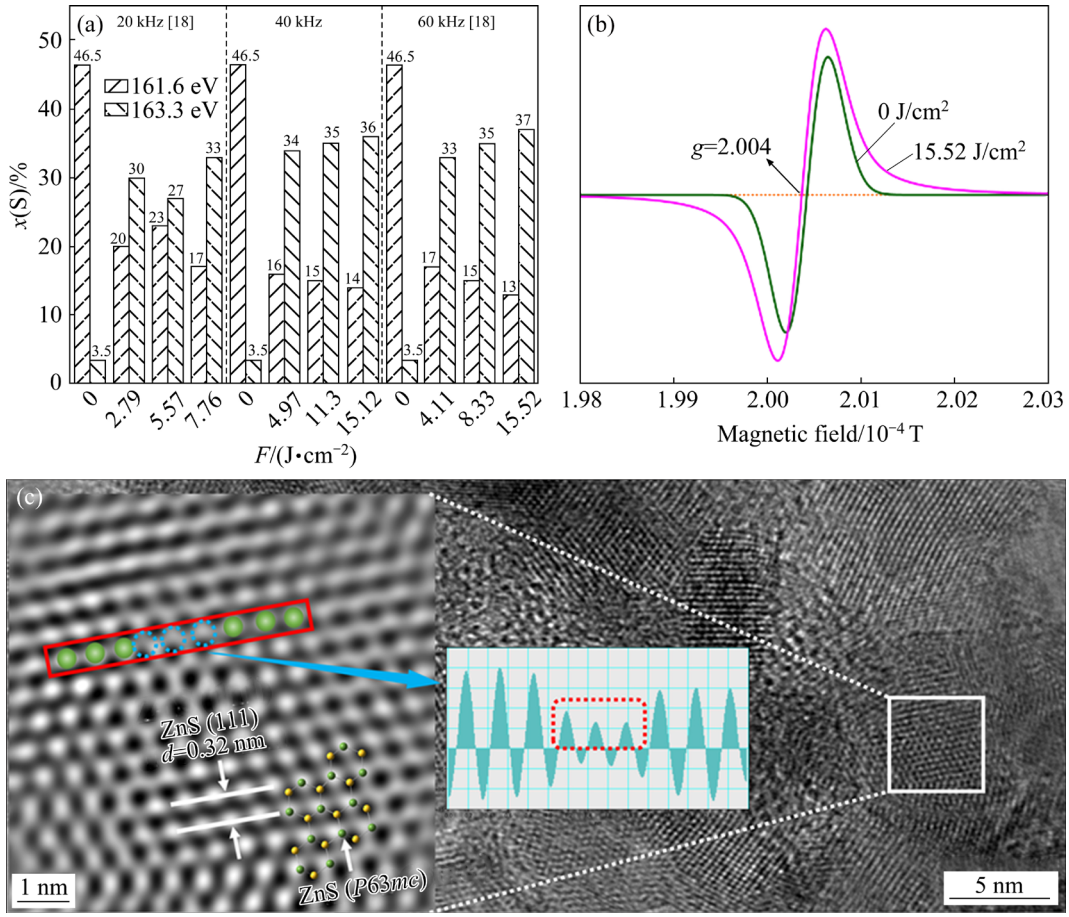

Fig. 4 (a) Diagram illustrating atomic fraction of spin-orbit splitting in S 2p region for different pulse repetition frequencies and laser fluences; (b) EPR spectra obtained for ZnS under different laser fluences; (c) HRTEM image of ZnS after laser irradiation: Zn atoms in green, and S atoms in yellow

S atoms are initially ejected, followed by a specific quantity of Zn^{2+} being ejected, which absorb photon energy, and combine with the electrons to produce Zn^0. Therefore, the formation of S vacancies indicated the occurrence of the laser-induced photodecomposition of ZnS, while the increase in the number of S vacancies enhanced the ejection of Zn^{2+} and increased the probability of Zn^{2+} combining with electrons to form Zn^0.

In Fig. 4(b), the horizontal coordinate represents the spectral splitting factor (g) and the vertical coordinate represents the signal intensity. The green curve represents the S defect content in unirradiated ZnS and the pink curve represents the S defect content in ZnS after laser irradiation with a laser fluence of 15.52 J/cm^2. All of the samples exhibited symmetric signals at a g-factor of 2.004, indicating the presence of S vacancies in the lattice of ZnS, which suggested that the paramagnetic signals in the ZnS lattice came from the unpaired electrons trapped in the S vacancies [29]. Meanwhile, upon comparing the vacancy concentrations, it was observed that the resonance signal at g=2.004 in the sample after laser irradiation was significantly stronger than that of the unirradiated sample ($1.516\times10^{11}>6.590\times10^{10}$), which indicated that laser irradiation of the ZnS surface generated more S vacancies.

HRTEM analysis of laser-irradiated ZnS revealed the formation of Zn defects during the interaction between ZnS and laser, as shown in Fig. 4(c). The measured lattice spacing (0.32 nm) corresponded to the (111) plane of ZnS. By measuring the intensity of the atomic peaks in the dotted red region, it was seen that the intensity of the middle three atomic peaks was relatively low, indicating that three atoms were missing from this position.

Figure S1 in SI shows the XRD pattern of the unirradiated ZnS, which revealed that the space group of the ZnS crystal structure was *P*63*mc* (186), which belonged to the hexagonal crystal system. By

matching the ZnS HRTEM map with its crystal structure, it was seen that the three missing atoms in the dotted red region were Zn atoms, suggesting that Zn defects were created on the ZnS surface after laser irradiation. Therefore, the presence of Zn defects confirmed the ejection of Zn^{2+} from the ZnS crystal upon laser irradiation, which combined with electrons to form Zn^0.

3.2 Effects of laser parameter on Zn^0 content generated

Three factors have an important impact on the Zn^0 content generated under laser irradiation: laser fluence (F), i.e. the energy value per unit area, pulse repetition frequency (f), i.e. the number of pulses output per unit time, and scan spacing. The scan spacing refers to the distance between the laser scanning lines, which also has an impact on the interaction between the laser and substrate material. A smaller scan spacing resulted in greater destructive effects on the material.

Figure 5 shows the valence distribution of Zn to explain the effect of laser parameters on the Zn^0 content generated. More evidence shows that Zn can generate Zn^0 upon laser irradiation as shown in Fig. S2 with more details given in Text S3 in SI. In

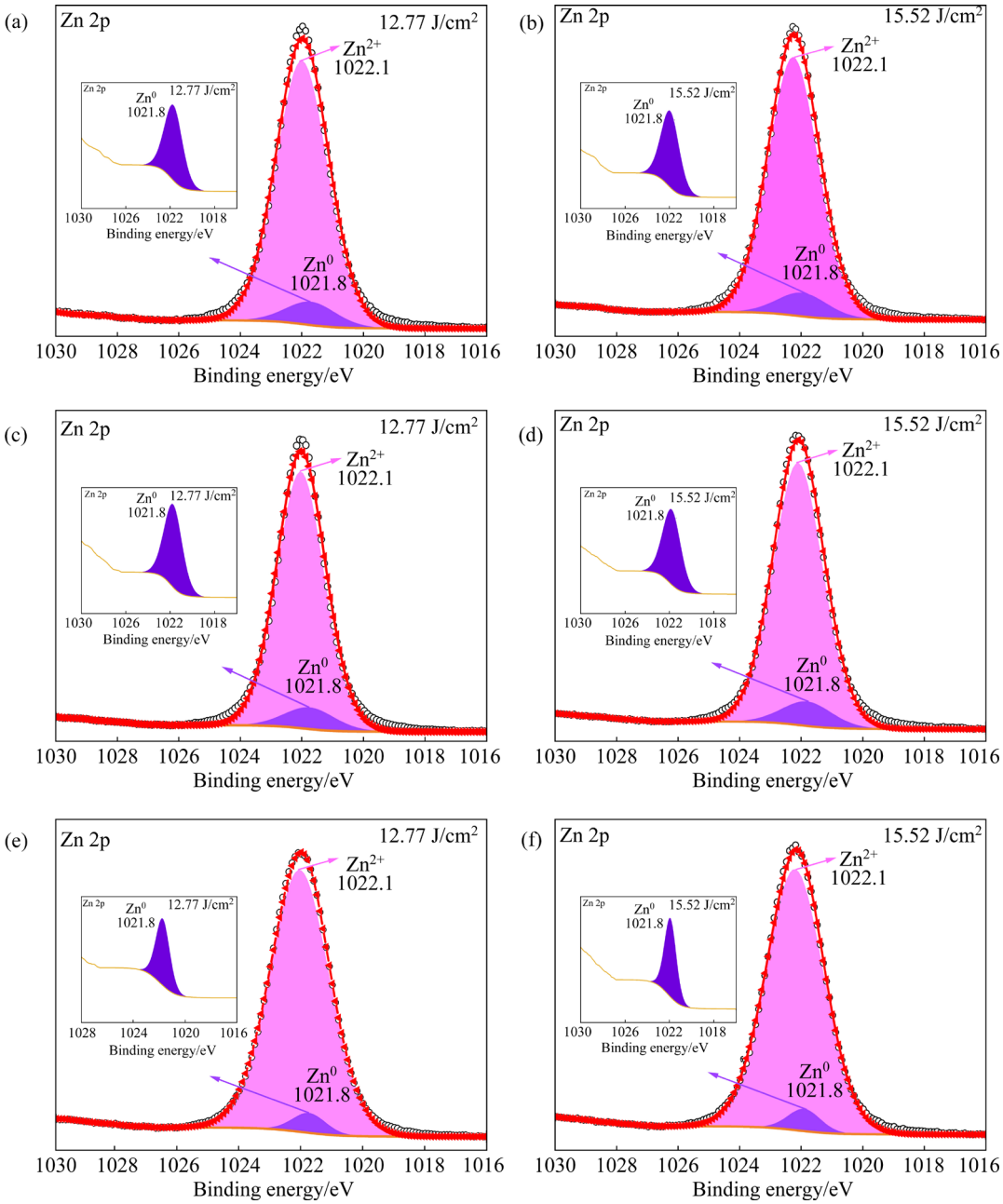

Fig. 5 XPS spectra obtained for Zn at different scan spacings and f of 60 kHz: (a, b) 0.01 mm; (c, d) 0.02 mm; (e, f) 0.03 mm

the Zn 2p region, the peaks were symmetrical with spin-orbit splitting [30]. The spin-orbit splitting for the peaks corresponding to Zn $2p_{3/2}$ and Zn $2p_{1/2}$ of ZnS was ~23 eV. Therefore, only the Zn $2p_{3/2}$ region was fitted with peak splitting in this study. The C 1s peak (284.8 eV) was used as a reference to calibrate all of the binding energies for all of the elements and details of the fitting parameters are given in Text S4 in SI.

Figures 5(a−e) show that the peaks observed in the Zn 2p XPS spectrum were assigned to two bonding types comprised of Zn−S (1022.1 eV) and Zn^0 (1021.8 eV), whose values were comparable to those reported in the NIST database [31]. Figure 5(f) shows that at F=15.52 J/cm^2, the peaks centered at 1021.8 and 1022.2 eV were ascribed to Zn^0 and Zn−S, respectively [32,33]. The results indicated that a certain amount of ZnS was photo-reduced to Zn^0 after laser decomposition. Details of the additional experimental confirmation of Zn^0 formation are presented in Text S5 in SI.

Quantitative analysis of the atomic ratios of surface Zn^0/Zn^{2+} under the different laser parameters was carried out, as shown in Fig. 6. According to Fig. 6(a), it can be observed that, when F and f were the same, the results obtained at a scan spacing of 0.01 and 0.02 mm provided almost identical Zn^0 contents in the laser-induced decomposition products of ZnS. When the scan spacing reached 0.03 mm, the Zn^0 content in the products decreased by half. This indicated that Zn^0 content in the products increased when the scan spacing was small. However, once it reached a certain level, further increasing the scan spacing led to an opposite effect on the production of Zn^0. This was attributed to when the scan spacing was relatively large, the increased distance between the scanning lines reduced the interaction area between the laser and the ZnS surface, leading to a decrease in the Zn^0 content.

Figure 6(b) shows under the same scan spacing and f, there was no generation of Zn^0 in the products when the F=4.11 J/cm^2. The Zn^0 content generated by laser irradiation at laser fluences of 12.77 and 15.52 J/cm^2 was nearly identical to that obtained at 8.33 J/cm^2, both accounting for ~8% of the Zn content. This indicated that the Zn^0 content did not increase significantly beyond F=8.33 J/cm^2. There was an optimal F value, ensuring the maximum Zn^0 content, while keeping the F at a relatively low level.

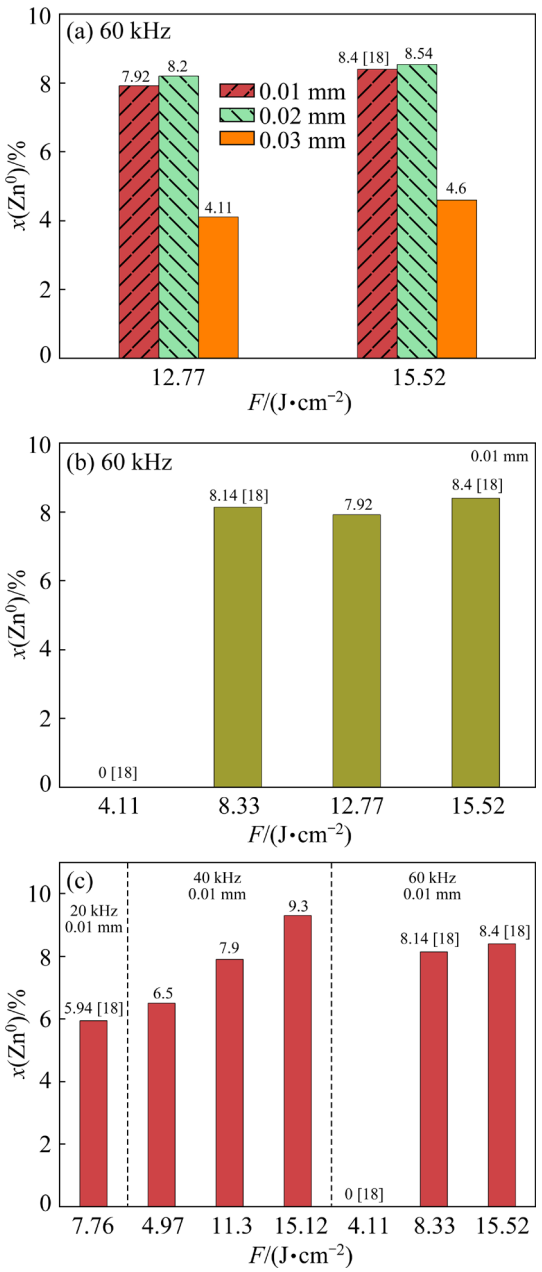

Fig. 6 Atomic ratios results for Zn^0 on ZnS: (a) Keeping f and F constant, while changing scan spacing; (b) Keeping f and scan spacing constant, while changing F; (c) Keeping F and scan spacing constant, while changing f

Therefore, Zn^0 occupied the largest percentage of the products, and the energy consumption of the laser was minimized when F=8.33 J/cm^2, f=60 kHz, and the scan spacing was 0.02 mm. When F reached a certain level, an increase in F did not significantly improve the Zn^0 content in the products. This was because when the F value was sufficient to break the chemical bonds in ZnS, it led

to its decomposition, and there was some generation of Zn^0 under the protection of an inert argon gas atmosphere. However, with further increases in F, some of the Zn^0 may transform into Zn vapor or a plasma state, which was challenging to detect on the surface of the ZnS crystal. Therefore, it was possible to increase the percentage of Zn^0 in the laser-induced decomposition products of ZnS by continuing to increase F.

The atomic ratios of Zn^{2+} and Zn^0 observed at different pulse repetition frequencies are illustrated in Fig. 6(c). Figure 6(c) shows the proportion of Zn^0 was 6.5% at similar F with f=40 kHz (4.97 J/cm^2), whereas there was no generation of Zn^0 in the products with f=60 kHz (4.11 J/cm^2). For laser fluences of 15.12 and 15.52 J/cm^2, the Zn^0 content in the products was 9.3% at f=40 kHz, while the Zn^0 content in the products was 8.4% at f=60 kHz. When the laser fluences were 7.76 and 8.33 J/cm^2, the Zn^0 content in the products was 6% at f=20 kHz, while the Zn^0 content was 8.1% at f=60 kHz.

Therefore, f had an effect on the laser-induced photoreduction reaction when the F and scan spacing were the same, which also had a relatively significant effect on the Zn^0 content in the products. When the laser power was equal, the number of pulses increased as f increased. However, the energy of single pulse irradiation decreased. If the laser power was relatively low, most of the pulse energy did not reach the damage threshold of the material. Therefore, the Zn^0 content was higher at f=40 kHz when compared to that at f=60 kHz for the reasons that when the laser fluences were similar, even though the number of pulses at 40 kHz was smaller than the number of pulses at 60 kHz, the pulses had high energy and both reached the damage threshold of ZnS, which better affected the surface of ZnS and led to an increased Zn^0 content. Multiple pulse energies were needed to reach the damage threshold of ZnS when f=60 kHz, resulting in a lower Zn^0 content.

The reason for the lower content of Zn^0 in the product at f=20 kHz when compared to that at f=60 kHz was that the number of pulses at 20 kHz was relatively small, despite the high energy per unit pulse at 20 kHz. This results in the number of pulses affecting the surface of ZnS being much smaller than those at f=60 kHz, leading to a reduction in the Zn^0 content. In conclusion, when f=40 kHz, the pulse number and pulse energy were suitable for the occurrence of the laser-induced photoreduction of ZnS, leading to the highest Zn^0 content.

Meanwhile, the Zn^0 content in the products reached a maximum of 9.3% when the laser-induced decomposition of ZnS was carried out at f=40 kHz, a scan spacing of 0.01 mm and F=15.12 J/cm^2. In the Raman spectrum of ZnS prepared at F=15.12 J/cm^2 (Fig. S4(c) in SI), there was a relatively obvious new peak appearing at 436 cm^{-1} after a few days of exposure to air when compared to that ZnS not exposed to air after being subjected to laser irradiation. The new peak was assigned to ZnO [34] and the peak intensity was stronger than the Raman peak intensity reported in previous studies [18].

3.3 Mechanism of Zn^0 generation using laser to irradiate ZnS

The laser-induced photoreduction technique was always accompanied by changes in the surface micromorphology that occur during the process of changing the chemical composition of ZnS. The microscopic morphology of the material surface played a crucial role in determining its surface chemical properties, such as material wettability, adsorption, adhesion, and corrosion resistance. Simultaneously, the interaction mechanism between the laser and materials had a significant influence on the formation of the material's surface microstructure.

Therefore, the interaction mechanism between laser and ZnS was elucidated by investigating the changes in the ZnS surface micromorphology under different laser parameters. The interaction mechanisms between the laser and materials mainly included the photothermal mechanism, photochemical mechanism, and the synergistic photothermal and photochemical mechanism [35]. The criterion for judgment from the microscopic topography was that if the material topography showed almost no molten morphology around the dot-like shallow pits in the material morphology image and no heat accumulation, which is consistent with the photochemical effect of the laser interaction with the material. If the topography showed a gradual deepening of the surface pits, a decrease in the amount of debris scattered on the surface, and the appearance of dot-like structures around the holes, which is consistent with the

photothermal effect [36,37]. The photothermal and photochemical effects between the materials and laser are shown in Fig. S5.

SEM shows the surface morphological characterization of ZnS obtained at different laser fluences and pulse repetition frequencies, as shown in Fig. 7(a). The ZnS surfaces exhibited the formation of pits with a certain depth. At lower F, the edges of the pits formed by laser-induced ablation were unclear. However, as F increased, the depth of the pits increased rapidly, followed by the edges becoming clearer and more uniform. The depth of the crater formed by the surface morphology of ZnS after the effect of different repetition frequencies and laser fluences in Fig. 7(a) was measured using a step profiler, and the specific results are shown in Fig. 7(b). Figure 7(b) shows when the laser fluences were similar but the pulse repetition frequencies varied, the depth of the craters increased with higher f.

Upon combining Figs. 7(a) with (b), there was no obvious spatter or melting at the edge of the crater when f=20 kHz. The cross-sectional profile of the structure was relatively smooth with no obvious areas of heating-induced curling or remelting. Our results showed that the laser had no obvious thermal damage in inducing the decomposition of ZnS, which means that the interaction mechanism between the laser and ZnS was mainly dominated by photochemical effects. When f=40 or 60 kHz, a small amount of debris was scattered on the surface with an increase in F, whereas a slight fluctuation was observed in the cross-sectional profile of the crater structure. This indicated that there was a partial photothermal effect in the interaction between the laser and ZnS, i.e. at low F, the interaction between the laser and ZnS was mainly through the photochemical effect, while at high F, a photothermal effect was generated. Therefore, the generation mechanism of Zn^0 in the products is a synergistic photochemical and photothermal effect.

The laser used in this study had a single photon energy of ~3.5 eV, which was close to the band gap of ZnS. Meanwhile, ZnS is a semiconductor and can take in the photon energy of a laser through either single-photon or two-photon absorption [38]. Photons, which serve as carriers of energy, transfer energy to the ZnS surface, where the free electrons absorb photon energy and undergo transitions. Under an inert argon atmosphere, the ionic bonds within the ZnS crystal are disrupted [18]. Later, Zn^{2+} within the crystal is ejected and forms bonds with electrons, resulting in the generation of Zn^0. Therefore, the generation mechanism for the direct photoreduction of ZnS to Zn^0 by laser-induced decomposition was a synergistic effect of photochemical and photothermal processes, with the photochemical process being predominant [39].

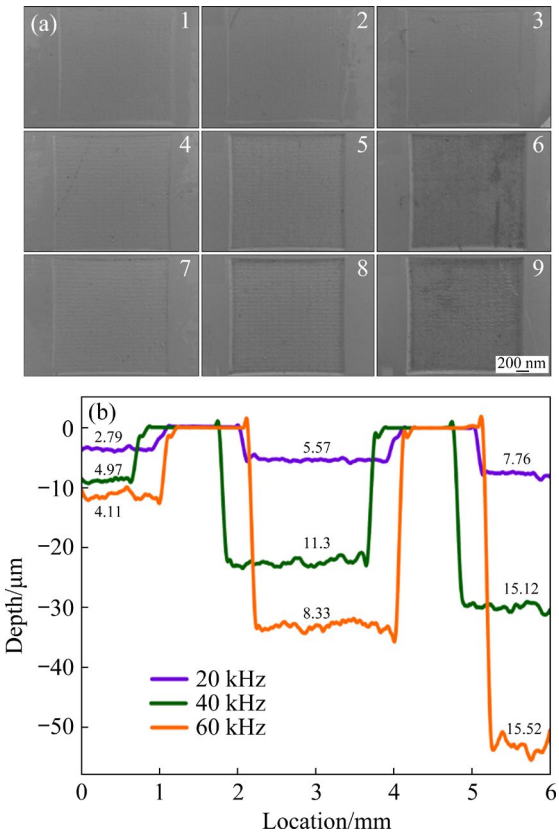

Fig. 7 (a) SEM images of ZnS surfaces after laser treatment at different pulse repetition frequencies and laser fluences: (1−3) f=20 kHz; laser fluences = 2.79, 5.57, and 7.76 J/cm^2, respectively, (4−6) f=40 kHz; laser fluences of 4.97, 11.3, and 15.12 J/cm^2, respectively, and (7−9) f=60 kHz; laser fluences of 4.11, 8.33, and 15.52 J/cm^2, respectively; (b) Cross-sectional profile of surface pit structures after interaction between laser and ZnS

The microstructure of ZnS was characterized before and after laser treatment, where the surface of the unirradiated ZnS (Fig. S6) was relatively smooth, with no obvious loose or spherical structures produced. At low F, as shown in Fig. S7, the morphology of ZnS after laser treatment exhibited a loose structure. With an increase in F, part of the ZnS structures transformed from a loose shape to a spherical shape. The reason for this was

that laser irradiation on the ZnS surface led to an increase in the local temperature, which excited surface vaporization and high-pressure plasma expansion. A large number of micro/nano particles were deposited via material ablation and plasma ejection due to this local temperature increase, which induces surface vaporization/ionization and high-pressure plasma expansion [40]. This process caused some of the ZnS to agglomerate into relatively regular spherical shapes.

Simultaneously, an increase in F led to a corresponding increase in the number of spherical structures. This was attributed to the irradiation of ZnS with different laser parameters leading to the difference in surface temperature, which was related to the wavelength, pulse width, scanning speed and F of the laser. Because the wavelength, pulse width, and scanning speed were kept constant in this experiment, the increase in F caused an increase in spherical structure at the same f.

4 Conclusions

(1) The exploration of the generation process of Zn^0 under laser irradiation revealed that the increase in S defects enhanced the ejection of Zn^{2+}, which increased the probability of Zn^{2+} combining with electrons to form Zn^0.

(2) The laser parameters, including f, F, and scan spacing had an effect on the Zn^0 content in the products, and there existed an optimal setting for each parameter, beyond which further increases or decreases in any parameter failed to enhance the proportion of Zn^0.

(3) By changing the laser parameters, a maximum Zn^0 content of 9.3% in the products was detected.

(4) The interaction mechanism between laser and ZnS was a synergistic effect of photochemical and photothermal processes, of which the photochemical mechanism predominates.

CRediT authorship contribution statement

Ying CHEN: Investigation, Validation, Data curation, and Writing − Original draft; **Ning DUAN:** Supervision, Conceptualization, Writing − Review & editing, and Funding acquisition; **Lin-hua JIANG:** Supervision, Writing − Review & editing, and Funding acquisition; **Hao JIN:** Resources, and Data curation; **Yao WANG:** Formal analysis; **Yong LIU:** Data curation.

Declaration of competing interest

The authors declare that they have no known competing financial interests or personal relationships that could have appeared to influence the work reported in this paper.

Supporting Information

Supporting Information in this paper can be found at: http://tnmsc.csu.edu.cn/download/20-p0613-2024-0787-Supporting_Information.pdf.

Acknowledgments

This research was financially supported by the Shanghai Leading Talent Project, China (No. 2022048), and the National Natural Science Foundation of China (No. 52174385).

References

[1] LIU Xiao-xiao, NIU Qian, DONG Shu-li, ZHONG Shui-ying. How does renewable energy consumption affect carbon emission intensity? Temporal-spatial impact analysis in China [J]. Energy, 2023, 284: 128690.

[2] SHANG M, PENG M Y, ANSER M K, IMRAN M, NASSANI A A, BINSAEED R H, ZAMAN K. Evaluating the U-shaped environmental Kuznets curve in China: The impact of high technology exports and renewable energy consumption on carbon emissions [J]. Gondwana Research, 2024, 127: 272−287.

[3] WANG Ya-hui, WU Ji-jun, HU Guo-chen, MA Wen-hui. Recovery of Li and Fe from spent lithium iron phosphate using organic acid leaching system [J]. Transactions of Nonferrous Metals Society of China, 2024, 34: 336−346.

[4] WANG Jun-bo, LIU Wei, CHEN Lu, LI Xin, WEN Zong-guo. Analysis of China's non-ferrous metals industry's path to peak carbon: A whole life cycle industry chain based on copper [J]. Science of the Total Environment, 2023, 892: 164454.

[5] LEVARD C, BARS M L, FORMENTINI T, LEGROS S, DOELSCH E. Organic waste-borne ZnS nanoparticles: The forgotten ones [J]. Environmental Pollution, 2022, 308: 119629.

[6] WANG Xin, SRINIVASAKANNAN C, DUAN Xin-hui, PENG Jin-hui, YANG Da-jin, JU Shao-hua. Leaching kinetics of zinc residues augmented with ultrasound [J]. Separation and Purification Technology, 2013, 115: 66−72.

[7] ZENG Yong, WANG Cui, HE Jian-feng, HUA Zhong-bao, CHENG Kai, WU Xi-qing, SUN Wei, WANG Li, HU Jia-cheng, TANG Hong-hu. Selective depressing mechanism of H-acid monosodium salt on flotation separation of graphite and sphalerite [J]. Transactions of Nonferrous Metals Society of China, 2023, 33: 3812−3824.

[8] WEI Qian, JIAO Fen, DONG Liu-yang, LIU Xue-duan, QIN Wen-qing. Selective depression of copper-activated sphalerite by polyaspartic acid during chalcopyrite flotation

[J]. Transactions of Nonferrous Metals Society of China, 2021, 31: 1784−1795.

[9] KOEPF E, ALXNEIT I, WIECKERT C, MEIER A. A review of high temperature solar driven reactor technology: 25 years of experience in research and development at the Paul Scherrer Institute [J]. Applied Energy, 2017, 188: 620−651.

[10] CHUAYBOON S, ABANADES S. Solar metallurgical process for high-purity Zn and syngas production using carbon or biomass feedstock in a flexible thermochemical reactor [J]. Chemical Engineering Science, 2023, 271: 118579.

[11] OMRAN M, FABRITIUS T, HEIKKINEN E, CHEN Guo. Dielectric properties and carbothermic reduction of zinc oxide and zinc ferrite by microwave heating [J]. Royal Society Open Science, 2017, 4: 170710.

[12] CHENG Ke-ke, YI Jia-fei, ZHA Guo-zheng, FAN Kai, LI Zi-cheng, KONG Xiang-feng, YANG Bin, XIONG Heng, XU Bao-qiang, JIANG Wen-long. Separation behavior of As, Zn and Cd trace impurities in the deep vacuum purification process of refined lead [J]. Separation and Purification Technology, 2021, 278: 119531.

[13] ZARZAR L D, SWARTZENTRUBER B S, HARPER J C, DUNPHY D R, BRINKER C J, AIZENBERG J, KAEHR B. Multiphoton lithography of nanocrystalline platinum and palladium for site-specific catalysis in 3D microenvironments [J]. Journal of the American Chemical Society, 2012, 134: 4007−4010.

[14] MARUO S, SAEKI T. Femtosecond laser direct writing of metallic microstructures by photoreduction of silver nitrate in a polymer matrix [J]. Optics Express, 2008, 16: 1174−1179.

[15] VORA K, KANG S Y, SHUKLA S, MAZUR E. Fabrication of disconnected three-dimensional silver nanostructures in a polymer matrix [J]. Applied Physics Letters, 2012, 100: 063120.

[16] DU Qing-zhi, REN En-yang. A new attempt of laser application-Laser metallurgy [J]. Journal of Kunming Institute of Technology, 1995, 20: 96. (in Chinese)

[17] JIANG Hao-qing, JIN Shen-yu, WANG Chao, MA Rui-qian, SONG Yin-yin, GAO Meng-yue, LIU Xing-tao, SHEN Ai-guo, CHEN G, DENG He-xiang. Nanoscale laser metallurgy and patterning in air using MOFs [J]. Journal of the American Chemical Society, 2019, 141: 5481−5489.

[18] CHEN Ying, DUAN Ning, JIANG Lin-hua, XU Fu-yuan, ZHU Gang-bin, WANG Yao, LIU Yong, CHENG Wen, XU Yan-li. Direct generation of Zn metal using laser-induced ZnS to eradicate carbon emissions from electrolysis Zn production [J]. Frontiers of Environmental Science & Engineering, 2023, 18: 7.

[19] LIU Yuan-yuan, ZHOU Yan-kai, ZHU Peng, LUO Xing-rui, CHEN Jie, LI Ying-ying, QIU Qing-qing, XIE Teng-feng. Surfactant-assisted synthesis of highly dispersed ZnS(C)/BiOBr/GO ternary composites for effectively improve the degradation ability of organic pollutants under visible light [J]. Journal of Molecular Liquids, 2023, 378: 121621.

[20] TANG Xi, WANG Yi-lin, LIU Zhi-fang, FEI Mao-heng, GAO Rong-huan, XIE Yi-xi, HU Xia-yi, ZHAO Peng-cheng, FEI Jun-jie. ZnS-assembled $CdIn_2S_4$ Z-type heterojunction as a photoelectrochemical sensor for ultra-trace detection of m-nitrophenol in environmental water samples [J]. Sensors and Actuators B: Chemical, 2024, 400: 134921.

[21] HUANG Zhi-dong, CAI Yu-kui, XUE Fei, HAN Yun-long, SONG Qing-hua, WANG Bing, LIU Zhan-qiang. Precise patterning of carbon films on polyethylene terephthalate polymer substrates using femtosecond lasers [J]. Applied Surface Science, 2023, 638: 158113.

[22] CHARLES K. Introduction to solid state physics [M]. The United States of America: Wiley, 2004.

[23] ZHENG Jing, YANG Biao, WANG Hu-jun, ZHOU Liu-cheng, ZHANG Zhi-hui, ZHOU Zhong-rong. Temperature-responsive, femtosecond laser-ablated ceramic surfaces with switchable wettability for on-demand droplet transfer [J]. ACS Applied Materials & Interfaces, 2023, 15: 13740−13752.

[24] WANG Qing-hua, YIN Kai, BAI Zong-chun, LIU Jian-long, HUO Lian-fei, WANG Hui-xin. Fabrication of robust superhydrophobic copper surface via highly efficient nanosecond laser-based surface functionalization [J]. Optik, 2023, 276: 170690.

[25] MENG A-lan, HUANG Tian-qi, LI Huan-yu, CHENG He, LIN Yu-sheng, ZHAO Jian, LI Zhen-jiang. Sulfur vacancies and morphology dependent sodium storage properties of MoS_{2-x} and its sodiation/desodiation mechanism [J]. Journal of Colloid and Interface Science, 2021, 589: 147−156.

[26] LOW Jing-xiang, DAI Ben-zhe, TONG Tong, JIANG Chuanjia, YU Jia-guo. In situ irradiated X-ray photoelectron spectroscopy investigation on a direct Z-scheme TiO_2/CdS composite film photocatalyst [J]. Advanced Materials, 2018, 31: 1802981.

[27] LIU Ying-chao, LI Yu-qiong, CHEN Jian-hua, KANG Duan, YANG Xi. Influence of sulfur vacancy on pyrite oxidization by water and oxygen molecules [J]. Colloids and Surfaces A: Physicochemical and Engineering Aspects, 2022, 634: 127954.

[28] ZHANG Chen, SHI Ying-zhang, WANG Zhi-wen, LIU Cheng, HOU Yi-dong, BI Jin-hong, WU Ling. Electrostatic interaction and surface S vacancies synergistically enhanced the photocatalytic degradation of ceftriaxone sodium [J]. Chemosphere, 2023, 311: 137053.

[29] LIU Guo, ZENG Qi, FAN Zi-ye, TIAN Shu-hao, LI Xi-juan, LV Xue-liang, ZHANG Wen-jian, TAO Kun, XIE Er-qing, ZHANG Zhen-xing. Boosting sulfur catalytic kinetics by defect engineering of vanadium disulfide for high-performance lithium-sulfur batteries [J]. Chemical Engineering Journal, 2022, 448: 137683.

[30] ESCAMILLA R, LÓPEZ ARANDA J A, CERVANTES J M, MUÑOZ H, LEÓN-FLORES J, ANTONIO J E, PILO J, ARÉVALO LÓPEZ E P, ROMERO M. Molten salts synthesis and Raman, XPS, and UV-vis spectroscopy study of Zn-doped $Y_2Ti_2O_{7-\delta}$ pyrochlore [J]. Ceramics International, 2024, 50: 15944−15951.

[31] WAGNER C D, NAUMKIN A V, ANNA K V, ALLISON J W, POWELL C J, RUMBLE J J R. NIST Standard Reference Database 20[S]. U. S. Department of Commerce, 2012.

[32] LU S W, SCHMIDT H K. Photoluminescence and XPS analyses of Mn^{2+} doped ZnS nanocrystals embedded in sol−gel derived hybrid coatings [J]. Materials Research Bulletin, 2008, 43: 583−589.

[33] MAENG J Y, YANG H J, JANG H J, JOO M H, KIM Y J, RHEE C K, SOHN Y. Electrocatalytic syngas and photo-catalytic long-chain hydrocarbon productions by CO_2 reduction over ZnO and Zn-based electrodes [J]. Applied Surface Science, 2023, 609: 155349.

[34] FU Yong-jun, WANG Zhi-chen, YOU Shao-qiang, ZHANG Rong-bin, WANG Xue-wen. Extraordinary photooxidation properties of ZnO nanosheets with surface oxygen vacancies of low density [J]. Applied Surface Science, 2023, 638: 158005.

[35] ARNOLD N, BITYURIN N, BÄUERLE D. Laser-induced thermal degradation and ablation of polymers: Bulk model [J]. Applied Surface Science, 1999, 138/139: 212−217.

[36] DU Qi-feng, CHEN Ting, LIU Jian-guo, ZENG Xiao-yan. Surface microstructure and chemistry of polyimide by single pulse ablation of picosecond laser [J]. Applied Surface Science, 2018, 434: 588−595.

[37] LIU Hui-long, MOON K S, LI Jia-xiong, XIE Ying-xi, LIU Jun-bo, SUN Zhi-jian, LU Long-sheng, TANG Yong, WONG Ching-ping. Laser-oxidized Fe_3O_4 nanoparticles anchored on 3D macroporous graphene flexible electrodes for ultrahigh-energy in-plane hybrid micro-supercapacitors [J]. Nano Energy, 2020, 77: 105058.

[38] KUMAR V P, PRADEEP C, SHA M M R, RADHAKRISHNAN P, MUJEEB A. Band-gap dependence of three-photon absorption in NiO nanoparticles synthesized at different calcination temperatures [J]. Optics & Laser Technology, 2023, 158: 108809.

[39] FENG Y, LIU Z Q, YI X S. Co-occurrence of photochemical and thermal effects during laser polymer ablation via a 248 nm excimer laser [J]. Applied Surface Science, 2000, 156: 177−182.

[40] LIU Chao, ZHENG Jun-jie, LIU Xiang-feng, YIN Kai, WANG Hui-xin, WANG Qing-hua. Facile laser-based process of superwetting zirconia ceramic with adjustable adhesion for self-cleaning and lossless droplet transfer [J]. Applied Surface Science, 2023, 638: 158069.

激光辐照 ZnS 直接生成金属锌的过程、影响因素及相互作用机理

陈 莹[1,2]，段 宁[1,2]，降林华[1,2]，金 浩[1,2]，王 垚[1,2]，刘 永[1,2]

1. 同济大学 环境科学与工程学院 污染控制与资源化研究国家重点实验室，上海 200092；
2. 上海污染控制与生态安全研究院，上海 200092

摘 要：研究金属锌(Zn^0)的生成过程、激光参数对 Zn^0 生成的影响以及激光与 ZnS 之间的相互作用机理。研究发现，S 缺陷的增加可提高 Zn^{2+}从 ZnS 晶体中被激发出的数量，从而增加 Zn^{2+}与自由电子结合生成 Zn^0 的概率。通过改变激光参数，产物中 Zn^0 的含量最高可达 9.3%。深入分析激光辐照 ZnS 后表面形貌的变化可知，激光与 ZnS 的相互作用机理为光化学与光热协同效应，其中光化学作用占主导地位。

关键词：激光冶金；硫缺陷；表面形貌；光化学还原；金属锌

(Edited by Xiang-qun LI)